Supplementary Information: "2D THz-THz-Raman Photon-Echo Spectroscopy of Molecular Vibrations in Liquid Bromoform"

Ian A. Finneran,[†,‡,§] Ralph Welsch,[†,‡,‖] Marco A. Allodi,[†,¶] Thomas F. Miller III,[†] and Geoffrey A. Blake[*,†,⊥]

†*Division of Chemistry & Chemical Engineering, California Institute of Technology, Pasadena, California 91125, USA*

‡*These authors contributed equally to this work*

¶*Current address: Department of Chemistry, The Institute for Biophysical Dynamics, and The James Franck Institute, The University of Chicago, Chicago, Illinois 60637, USA*

§*Current address: JILA, National Institute of Standards and Technology, University of Colorado, Boulder, Colorado 80309, USA*

‖*Current address: Center for Free-Electron Laser Science, DESY, Notkestraße 85, D-22607 Hamburg, Germany*

⊥*Division of Geological & Planetary Sciences, California Institute of Technology, Pasadena, California 91125, USA*

E-mail: gab@gps.caltech.edu

Experimental Setup

The broadband 2D THz-THz-Raman experiment is shown in Fig. S1, and is based on our previous work.[1,2] Two linearly polarized THz pulses are generated from the signal and idler output of an ultrafast optical parametric amplifier (OPA) incident on two DSTMS THz emitters. The THz pulse generated by the signal branch of the OPA is vertically polarized, while the idler-driven THz pulse is horizontally polarized. A THz wiregrid polarizer is used to combine the two THz beams in a collinear geometry, which improves the beam overlap and co-propagation of the two THz pulses. Residual near-IR light in the THz path is blocked with a roughened TOPAS plate along with several thin layers of black polyethylene. We have confirmed the effectiveness of this near-IR beam block with a pyroelectric detector (Scientech 361). The THz pulses are sent through a 7.5:1 Gaussian telescope, and then focused on the sample. The THz field strength at the sample is $\sim$300 kV/cm.[2] The Raman probe pulse ($\sim$1 μJ, 38 fs, vertically polarized) is generated from the same laser system and focused on the sample collinear to the THz beams. Heterodyne detection of the Raman probe pulse increases the signal-to-noise ratio and allows for phase-sensitive detection of the 2D TTR response.

Liquid samples are held in a Suprasil quartz cuvette with a front facing diamond window (Fig. S1b). The diamond window allows broadband THz transmission to the liquid sample, while the 800 nm Raman probe passes freely through the diamond window, liquid, and back Suprasil quartz window.

Data Analysis

The raw 2D TTR data from liquid bromoform are shown in Fig. S2a. The acquisition time step is <1 fs for t_2 and 50 fs for t_1. Additional data with a t_1 acquisition time step of 25 fs was taken on diamond to determine the instrument response (Fig. 2 in the main text), and on liquid bromoform to rule out aliasing in the 2D spectrum. The sampling windows

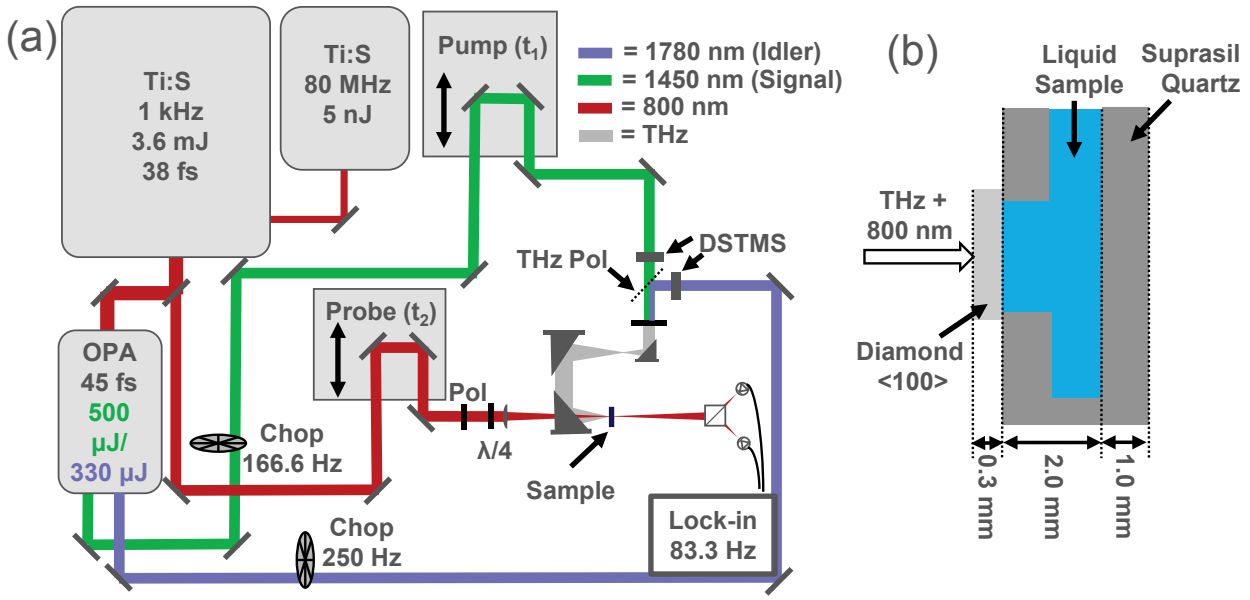

Figure S1: (a) A diagram of the broadband 2D TTR experiment. A THz wiregrid polarizer (labeled 'THz Pol') is used to combine the THz beams. (b) Details of the sample cuvette used in the instrument. The front facing diamond window allows broadband THz transmission to the liquid sample. Both the diamond and Suprasil quartz are transparent to the 800 nm Raman probe pulse.

for bromoform are -1.5 to 2.2 ps for t_1 and -0.5 to 5.0 ps for t_2. We observed no etalons in these time windows.

The orientational response is detrended out with a single exponential fit, as shown in a previous publication.[1] This isolates the vibrational coherences on the t_1 and t_2 axes (Fig. S2b). The rephasing and non-rephasing contributions to the signal are extracted with a 2D complex Fast Fourier Transform (FFT) of the total signal. The rephasing contribution is obtained by setting values in the first and third quadrant of the complex FFT to zero and then applying an inverse FFT back to the time domain (Fig. S2c). Likewise, the non-rephasing contribution is generated by setting the second and fourth quadrant to zero and applying an inverse FFT back to the time domain (Fig. S2).

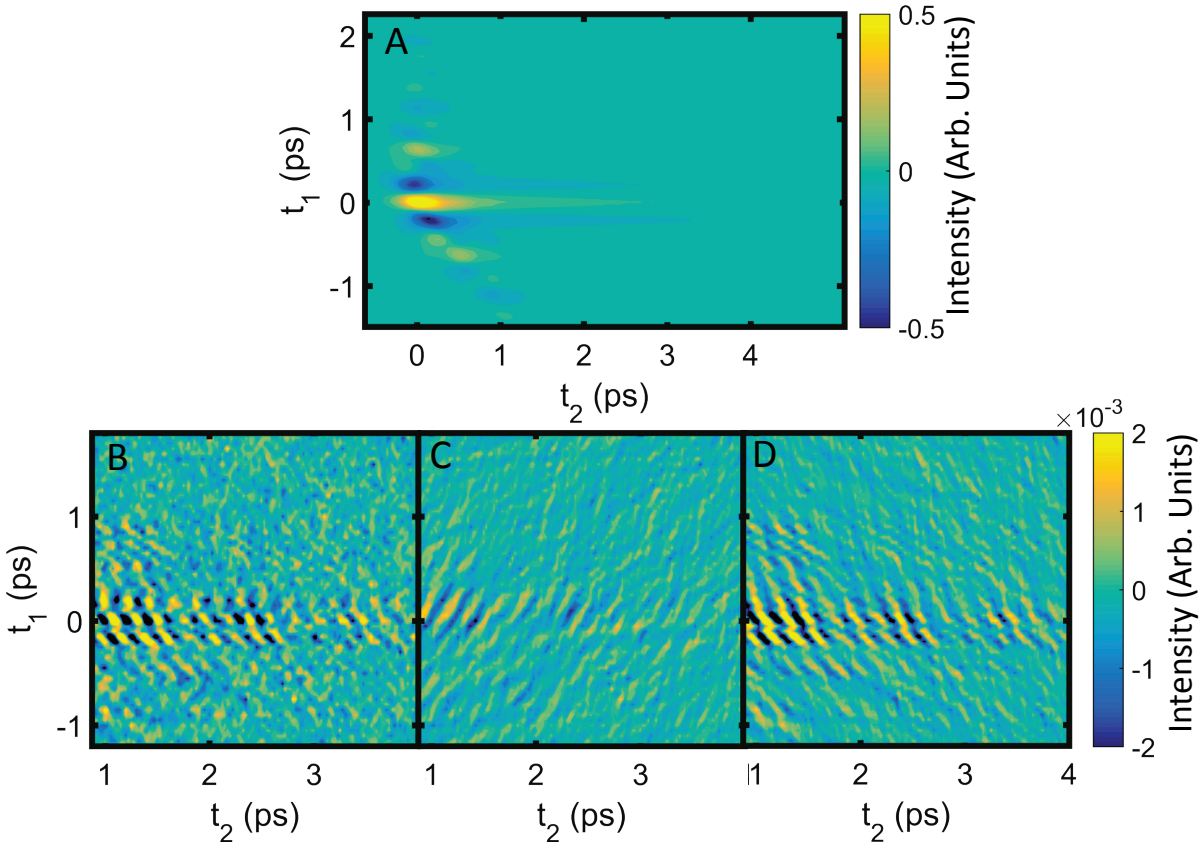

Figure S2: (a) The 2D TTR response of bromoform. (b) Detrending the orientational response and shifting to larger t_2 values isolates the vibrational coherences. (c) The rephasing portion of the vibrational coherences. (d) The non-rephasing portion of the vibrational coherences.

Reduced Density Matrix Modeling

Model Details

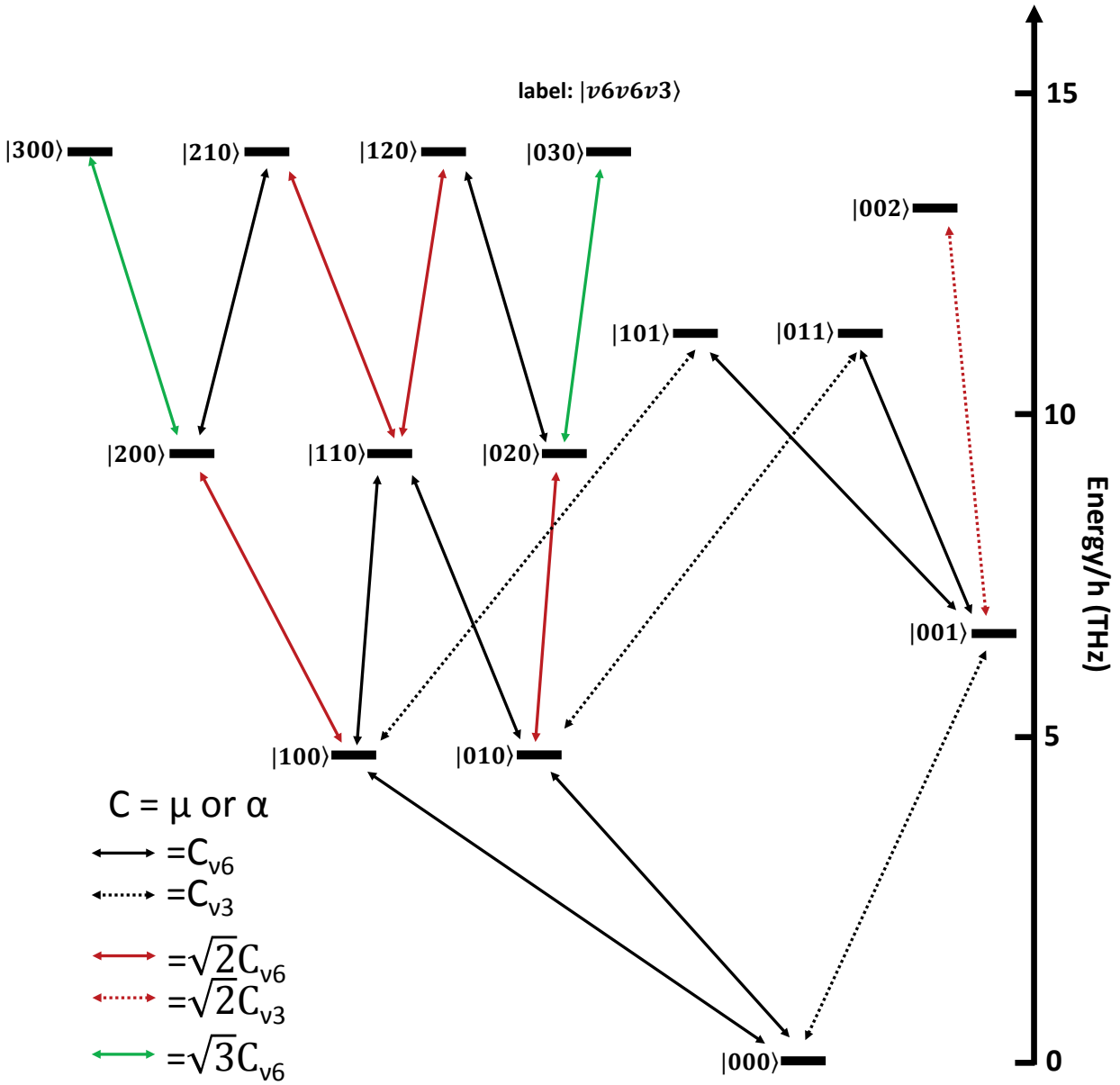

Figure S3: A schematic of the fixed coupling elements in the RDM fits.

The simulation fits of the 2D TTR spectrum were carried out with a reduced density matrix (RDM) model described in our previous work.[1] The time evolution of the density

matrix $\boldsymbol{\rho}$ is determined by the Liouville-Von Neumann equation

$$i\hbar\frac{\partial\boldsymbol{\rho}}{\partial t}=\left[\boldsymbol{H},\boldsymbol{\rho}\right], \tag{1}$$

where $\boldsymbol{H}$ is the Hamiltonian operator. We use a second-order differencing technique[3] to numerically calculate the time evolution of the density matrix:

$$\boldsymbol{\rho}\left(t+\Delta t\right)=\boldsymbol{\rho}\left(t\right)-\frac{i}{\hbar}\ \left[\boldsymbol{H}\left(t\right),\boldsymbol{\rho}\left(t\right)\right]\ 2\ \Delta t-2\boldsymbol{\Gamma}\ \Delta t\boldsymbol{\rho}(t), \tag{2}$$

where $\Gamma_{i,j}=(1-\delta_{i,j})\frac{1}{\tau_{i,j}}$ is the dephasing rate with an associated time constant $\tau_{i,j}$.[4,5]

The Hamiltonian $\boldsymbol{H}\left(t\right)$ consists of time-independent $\boldsymbol{H}^0$ and time-dependent $\boldsymbol{H}^L(t)$ terms, which respectively describe the molecular system and its interaction with the THz pulses:

$$H^0_{i,j}=E_i\delta_{i,j}, \tag{3}$$

$$H^L_{i,j}(t)=\mu_{i,j}F(t). \tag{4}$$

Here, E_i is the energy of the i-th system eigenstate, $\mu_{i,j}$ is the dipole coupling element between state i and j, and the THz electric field $F(t)$ is given as

$$F(t)=A\sum_{i=1,2}\mathrm{e}^{\frac{-(t-\tau_i)^2}{2\sigma_i^2}}\cos(\omega_i(t-\tau_i)), \tag{5}$$

where τ_i, σ_i, and ω_i are the temporal delay, the temporal width, and center frequency of the i-th THz pulse, respectively, and A is the THz electric field strength of both pulses.

The nonlinear molecular polarization corresponding to the measured signal is given by

$$P(t)=\mathrm{tr}\left(\boldsymbol{D}\ \boldsymbol{\rho}(t)\right)-\sum_{j=1,2}\mathrm{tr}\left(\boldsymbol{D}\boldsymbol{\rho_j}(t)\right), \tag{6}$$

where the matrix $\boldsymbol{D}$ contains coupling elements for the final Raman interaction and $\boldsymbol{\rho}_j(t)$ is

propagated with only the j-th THz pulse. We subtract the single pulse responses from the total response to isolate the two pulse nonlinear response of the system. In the experiment, this is accomplished with differential chopping of the two THz beams. To generate the 2D response, the first THz pulse is fixed at $\tau_1 = 0.0$ fs, the second pulse is scanned as $t_1 = -\tau_2$, and the Raman readout delay is given as $t_2 = t$. 2D spectra were generated by applying a 2D FFT to the resulting 2D response. Simulations were only run for $\tau_2 > \sigma_1$, since this model does not properly describe the system response when the THz pulses are fully overlapped in the time domain.

Table S1: Summary of general parameters used in the density matrix propagation.

τ_1 in fs	0.0
τ_2 in fs	-300 – -2000
$\Delta\tau_2$ in fs	50
σ_1 in fs	150
σ_2 in fs	150
ω_1 in THz	2.5
ω_2 in THz	2.5
$\tau_{i,j}$ in fs	1500
t_s in fs	-4000
t_e in fs	4000
Δt in fs	1.0

Application of the RDM Model to the $\nu 3$ and $\nu 6$ Vibrations of Bromoform

Transition dipole and polarizability matrix elements employed in the RDM model are the square root of the respective IR- and Raman-intensities[6]

$$I_{j\to i}^{\mathrm{IR}} = A\left|\langle \Psi_i \left|\vec{\mu}\right| \Psi_j\rangle\right|^2, \tag{7}$$

$$I_{j\to i}^{\mathrm{Raman}} = B\left|\frac{\gamma_{ij}}{15}\right|^2, \tag{8}$$

$$\gamma_{ij} = \frac{1}{2}\left((\alpha_{ij}^{xx}-\alpha_{ij}^{yy})^2+(\alpha_{ij}^{yy}-\alpha_{ij}^{zz})^2+(\alpha_{ij}^{zz}-\alpha_{ij}^{xx})^2+3.0\left(\alpha_{ij}^{xy^2}+\alpha_{ij}^{xz^2}+\alpha_{ij}^{yz^2}\right)\right), \tag{9}$$

$$\alpha_{ij}^{ab} = \langle \Psi_i \left|\alpha_{ab}\right| \Psi_j\rangle, \tag{10}$$

where Ψ_j and Ψ_i are the initial and final vibrational states, respectively, $\vec{\mu}$ is the dipole and α_{ab} the polarizability operator, and A and B appropriate normalization constants, which will be neglected as they cancel in the RDM description due to the normalization of all matrix elements.

To apply the RDM model to bromoform, we included vibrational eigenstates and their associated dipole and polarizability coupling elements up to E/h=15 THz. The 1-quantum couplings were fixed at values expected of a harmonic oscillator for dipole transitions: $\mu_{n-1,n} = \sqrt{n}\mu_{0,1}$ and polarizability transitions: $\alpha_{n-1,n} = \sqrt{n}\alpha_{0,1}$. Here, $\mu_{0,1}$ and $\alpha_{0,1}$ are the dipole and polarizability coupling elements of the fundamental transitions, respectively. A full schematic of the fixed 1-quantum coupling elements is given in Fig. S3.

The relative intensities of the transition dipole moments of the $\nu 3$ ($\mu_{\nu 3}$) and $\nu 6$ ($\mu_{\nu 6}$) fundamentals were calculated using the ratio of the integrated intensities of the two modes in the linear spectrum. From our previous linear data,[1] the ratio of the integrated intensities is $I_{\nu 3}/I_{\nu 6}$ =1.1(1), in agreement with the literature values[7] $I_{\nu 3}/I_{\nu 6}$ =1.2. Using our ratio and a temperature of 295 K, the dipole coupling ratio is calculated from

$$\frac{I_{\nu 3}}{I_{\nu 6}} = \frac{\sum_{\nu 3} |n^{1/2}\mu_{\nu 3}|^2 \Delta N_n}{\sum_{\nu 6} |m^{1/2}\mu_{\nu 6}|^2 \Delta N_m} = \frac{|\mu_{\nu 3}|^2 \sum_{\nu 3} n\Delta N_n}{|\mu_{\nu 6}|^2 \sum_{\nu 6} m\Delta N_m}. \tag{11}$$

The sums are performed over all of the thermally populated 1-quantum transitions (including hot bands) of $\nu 3$ and $\nu 6$. We truncate this sum at 15 THz of total energy. The n indices indicate the number of $\nu 3$ quanta in the upper state and the m indices the number of $\nu 6$ quanta in the upper state. For each transition, ΔN is the difference in population between the two states involved in each transition. We have also assumed the harmonic oscillator approximation, with the relative transition dipoles of the hot bands given by $m^{1/2}\mu_{\nu 6}$ for $\nu 6$ and $n^{1/2}\mu_{\nu 3}$ for $\nu 3$, where $\mu_{\nu 6}$ and $\mu_{\nu 3}$ are the fundamental transition dipole moments of the two modes. Rearranging this equation we find

$$\frac{\mu_{\nu 3}}{\mu_{\nu 6}} = \left(\frac{I_{\nu 3} \sum_{\nu 6} m\Delta N_m}{I_{\nu 6} \sum_{\nu 3} n\Delta N_n} \right)^{1/2} \approx 1.6. \tag{12}$$

Table S2: Eigenstate energies (E), and degeneracies (g) used in the calculations.

State	E (THz)	g
$\|00\rangle$	0.0	1
$\|10\rangle$	4.7	2
$\|01\rangle$	6.6	1
$\|20\rangle$	9.4	3
$\|11\rangle$	11.3	2
$\|02\rangle$	13.2	1
$\|30\rangle$	14.1	4

For the polarizability couplings, the $\nu 6$ ($\alpha_{\nu 6}$) fundamental was fixed and the relative intensity of $\nu 3$ ($\alpha_{\nu 3}$), R, was fit. In this case, $\alpha_{\nu 3}$ is expected to be smaller than $\alpha_{\nu 6}$, since $\nu 6$ is depolarized, $\nu 3$ is polarized, and the Raman probe detection is depolarized. Couplings larger than 9.5 THz were set to zero.

The eigenstate energies were initialized from our previous linear spectrum with $\nu 6$=4.76 and $\nu 3$=6.68 and manually varied by the experimental error of $\pm$0.1 THz. Combination, overtone, and difference bands were determined assuming zero vibrational anharmonicity (equal spacing between eigenstates in a particular manifold), as shown in Table S2.

Incorporation of the Fitness Function with the RDM Model

The fitness of each RDM simulated spectrum was computed using the fitness function:

$$F = \sqrt{\sum_i (E_i - S_i)^2}, \tag{13}$$

where E_i are the points in the experimental spectrum, S_i are the corresponding points in the simulated spectrum, and the summation is performed over all points in the 2D spectrum. Each simulated and experimental spectrum was normalized to a maximum signal of 1.0 arbitrary units before this calculation. Regularization was also applied to the fitness function to prevent overfitting of the data:

$$F' = F + \alpha|\mathbf{K}|, \tag{14}$$

where α is the regularization parameter and $\mathbf{K}$ is a vector containing all of the multi-quantum coupling elements. The value of α was maximized to penalize large coupling values, without compromising the agreement between the simulated and experimental spectra. All multi-quantum polarizability and dipole couplings were initialized to random values between 0.0-1.0 arbitrary units and constrained to this same range in the fit. Initially, a basin-hopping minimization[8] was run 10 times with random initializations to check the robustness of the fit. A 'temperature' parameter of 0.1 and 10 total basin hopping iterations were used in each run. Then, the coupling elements were further optimized with a quasi-newton SLSQP local minimizer.[9]

RDM Fit Results

The final fit of the dipole and polarizability coupling elements is shown in Tables S3 and S4. To confirm that the fit had converged, we calculated the Hessian of the fitness function and verified that there were no negative eigenvalues. The uncertainties of the fit were determined from the covariance matrix, calculated by inverting the Hessian.

Table S3: Calculated and fit dipole matrix elements relative to $\mu_{|000\rangle,|100\rangle}$. All calculated results are for isolated bromoform monomers. In the experimental fits, all couplings that connect states of the same energy and change in quanta were constrained to the same value (e.g. $\mu_{|001\rangle,|200\rangle}$, $\mu_{|001\rangle,|110\rangle}$, $\mu_{|001\rangle,|020\rangle}$).

States	Quanta	HF	MP2	CCSD	DID	RDM Fit
$\|0\ 0\ 0\rangle$, $\|1\ 0\ 0\rangle$	1	1.00	1.00	1.00	1.00	1.00 (fixed)
$\|0\ 0\ 0\rangle$, $\|0\ 0\ 1\rangle$	1	1.34	1.00	1.01	1.14	1.60 (fixed)
$\|1\ 0\ 0\rangle$, $\|0\ 0\ 1\rangle$	2	0.04	0.03	0.04	0.00	0.009(5)
$\|2\ 0\ 0\rangle$, $\|1\ 0\ 1\rangle$	2	0.06	0.04	0.06	0.00	0.000(4)
$\|1\ 0\ 1\rangle$, $\|0\ 0\ 2\rangle$	2	0.06	0.04	0.06	0.00	0.000(3)
$\|1\ 0\ 0\rangle$, $\|0\ 0\ 2\rangle$	3	0.00	0.00	0.00	0.00	0.36(4)
$\|0\ 0\ 1\rangle$, $\|2\ 0\ 0\rangle$	3	0.01	0.02	0.01	0.00	0.44(2)
$\|1\ 0\ 1\rangle$, $\|3\ 0\ 0\rangle$	3	0.01	0.03	0.02	0.00	0.03(4)
$\|0\ 0\ 1\rangle$, $\|3\ 0\ 0\rangle$	4	-	-	-	-	0.023(5)
$\|2\ 0\ 0\rangle$, $\|0\ 0\ 2\rangle$	4	-	-	-	-	0.09(2)

Coherence Transfer

A possible source of forbidden transitions in 2D TTR spectra is coherence transfer and population transfer processes, which have been observed in 2D infrared spectra.[10] These processes are intermolecular in nature, and result from the coupling of molecular vibrations with the surrounding solvent 'bath' modes of the liquid. This coupling allows for the spontaneous transfer of coherences and populations within the density matrix of the system, without the loss of phase memory. The energies of the transfers are limited to that available from the surrounding bath, or $\sim k$T.[11] We note that these processes lead to the appearance of 'forbidden' multi-quantum transitions via dynamical processes, not to their direct excitation during the light-matter interaction via modifications of the dipole and/or polarizability surfaces. This includes transitions forbidden in the harmonic approximation as well those that are symmetry forbidden. Coherence transfer typically arises in the context of waiting-time measurements, which would be possible in a 2D THz-THz-THz experiment (analogous to 2D IR).[10]

We generalized the RDM model described in Eq.(2) to include coherence transfer via inclusion of more terms in the (Redfield) relaxation tensor $\mathbf{\Gamma}$:[10]

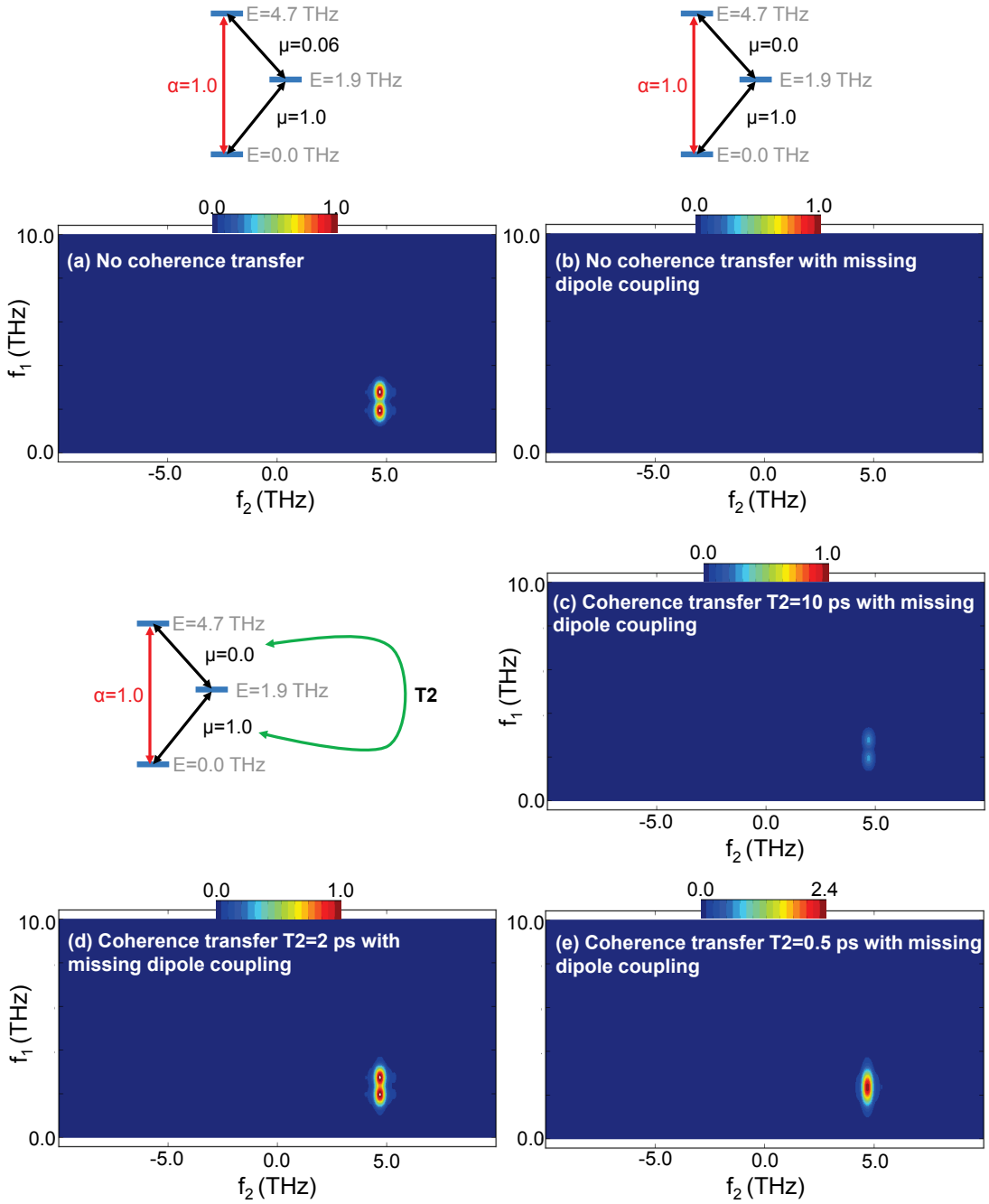

Figure S4: A coherence transfer simple model using three eigenstates. (a) In a closed three level system with no coherence transfer, a doublet pattern is generated in the 2D TTR spectrum. (b) If one of the dipole coupling elements is set to zero, then no 2D TTR pathways are possible. (c) If a 10 ps coherence transfer is added to the system, the doublet pattern returns. (d) The doublet pattern increases in intensity for shorter coherence transfer times, but becomes motionally narrowed into a single peak (e) for times shorter than the measurement time (∼2 ps).

Table S4: Calculated and fit polarizability matrix elements relative to $\alpha_{|000\rangle,|100\rangle}$. All calculated results are for isolated bromoform monomers. The CCSD polarizabilities are obtained by numerical differentiating the dipole moments with respect to an external electric field. In the experimental fits, all couplings that connect states of the same energy and change in quanta were constrained to the same value (e.g. $\alpha_{|001\rangle,|200\rangle}$, $\alpha_{|001\rangle,|110\rangle}$, $\alpha_{|001\rangle,|020\rangle}$). *This coupling was not well determined in the fit.

States	Quanta	HF	MP2	CCSD (num.)	DID	RDM Fit
$\|0\ 0\ 0\rangle$, $\|1\ 0\ 0\rangle$	1	1.00	1.00	1.00	1.00	1.00 (fixed)
$\|0\ 0\ 0\rangle$, $\|0\ 0\ 1\rangle$	1	0.92	0.80	0.84	0.06	0.048(1)
$\|1\ 0\ 0\rangle$, $\|0\ 0\ 1\rangle$	2	0.02	0.02	0.02	0.01	0.000(3)
$\|2\ 0\ 0\rangle$, $\|1\ 0\ 1\rangle$	2	0.03	0.03	0.03	0.01	0.001(3)
$\|1\ 0\ 1\rangle$, $\|0\ 0\ 2\rangle$	2	0.03	0.03	0.03	0.01	0.000(3)
$\|1\ 0\ 0\rangle$, $\|0\ 0\ 2\rangle$	3	0.00	0.00	0.03	0.00	0.000(4)
$\|0\ 0\ 1\rangle$, $\|2\ 0\ 0\rangle$	3	0.00	0.00	0.01	0.00	0.019(8)
$\|1\ 0\ 1\rangle$, $\|3\ 0\ 0\rangle$	3	0.00	0.00	0.01	0.00	0.000*
$\|0\ 0\ 1\rangle$, $\|3\ 0\ 0\rangle$	4	-	-	-	-	0.000(3)
$\|2\ 0\ 0\rangle$, $\|0\ 0\ 2\rangle$	4	-	-	-	-	0.004(3)

$$\frac{\partial \rho_{ij}}{\partial t} = -i\omega_{ij}\rho_{ij} + \sum_{kl} \Gamma_{ij,kl}\rho_{kl}. \tag{15}$$

Here, ω_{ij} is the transition frequency between states i and j. This expression is written in terms of the vibrational eigenstates of the molecular Hamiltonian (i,j,k,l). Relaxation tensor elements of the form $\Gamma_{ij,kl}$ correspond to coherence transfer, $\Gamma_{ii,jj}$ to population transfer, $\Gamma_{ii,ii}$ to population relaxation, and $\Gamma_{ij,ij}$ to dephasing, which was included in Eq. (1).

Simulations of coherence transfer in a simple model three-level system using the updated RDM code are shown in Fig. S4. We found that the model is only sensitive to coherence transfer and not to population transfer, due to the fact that all of the intermediate states in 2D TTR are coherences (off-diagonal in the density matrix). In Fig. S4(a) we simulated a standard three-level system that gives rise to the doublet pattern in bromoform (feature VII and VIII in Fig. 3(a) of the main text). If one of the dipole couplings is set to zero (Fig. S4(b)) then no peaks are present, as expected. However, if we introduce a coherence

transfer timescale T2=$1/\Gamma_{ab,bc}$ into the system, the doublet pattern returns. The doublet intensity increases for shorter T2 timescales, but eventually becomes motionally narrowed for timescales <1 ps and blends into a single peak. These results are quite promising, as they demonstrate how coherence transfer processes can connect a triad of eigenstates with missing or 'forbidden' connections. However, further simulations and fits using the full set of bromoform eigenstates were unable to reproduce the experimental results. Thus, coherence transfer does not seem to be a dominant effect in the bromoform spectrum, although it may be significant in other systems.

Anharmonic Vibrational Calculations

Anharmonic vibrational states were calculated employing vibrational second-order perturbation theory (VPT2)[12–14] as implemented in the Gaussian 16 package.[15] Electronic structure calculations are performed at the Hatree-Fock (HF) and second-order Møller-Plesset perturbation theory (MP2) level employing an augmented triple zeta basis set developed by Dunning (aug-cc-pVTZ).[16] To check the stability of the results, simulations explicitly employing symmetry and explicitly not employing symmetry are performed. As both match for the quantities shown below, only results employing symmetry are given. The frequencies and IR intensities of the relevant modes are given in Tab. S5 and compared to harmonic results. The anharmonic and harmonic frequencies are in very good agreement indicating small mechanical anharmonicity. The harmonic and anharmonic IR intensities differ by less than 12 % and their relative value by 5 %.

Due to numerical instabilities in the calculations and the small magnitude of the multi-quantum IR intensities, no IR intensities for multi-quantum transitions are given. However, the calculation of excitation energies for states with up to two quanta in energy in the relevant modes show less than three cm^{-1} difference to the corresponding harmonic values, which again indicates very small (mechanical) anharmonicity.

Table S5: Calculated excitation energies (in cm^{-1}) of vibrational states and corresponding IR intensities (in km/mol) including anharmonicities employing VPT2 and HF/aug-cc-pVTZ. For comparison, harmonic values are given too.

States	Quanta	E (harm.)	IR (harm.)	E (anharm.)	IR (anharm.)
$\|0\ 0\ 0\rangle$, $\|1\ 0\ 0\rangle$	1	167	0.016	167	0.014
$\|0\ 0\ 0\rangle$, $\|0\ 0\ 1\rangle$	1	242	0.029	241	0.027

Calculation of Dipole and Polarizability Non-Linearities

Ab initio electronic structure calculations and molecular dynamics (MD) simulations were performed to explore the possible molecular origin of non-linearities of the transition dipole and polarizability matrix elements. First, the approach for calculating the matrix elements employed in the RDM model from both *ab initio* electronic structure calculations and MD simulations is described. Second, the numerical details of the performed calculations are given. Third, the results for the different approaches are discussed.

Calculation of Transition Dipole and Polarizability Matrix Elements for the RDM Model

Transition dipole and polarizability matrix elements employed in the RDM model are the square root of the respective IR- and Raman-intensities (see. Eqs. 7 and 8) and thus proportional to $\langle \Psi_i \left| \vec{\mu} \right| \Psi_j \rangle$ and $\langle \Psi_i \left| \alpha_{ab} \right| \Psi_j \rangle$, respectively. In the following, the steps to obtain dipole matrix elements $\langle \Psi_i \left| \vec{\mu} \right| \Psi_j \rangle$ from both *ab initio* calculations and a DID model are discussed. The same steps are also employed to obtain the polarizability matrix elements $\langle \Psi_i \left| \alpha_{ab} \right| \Psi_j \rangle$. Only the three lowest energy vibrational normal modes of bromoform are considered, and as discussed in the main text, the PES with respect to these motions is

assumed to be harmonic. Therefore, $\langle \Psi_i \left| \vec{\mu} \right| \Psi_j \rangle$ is expanded as

$$\langle \Psi_i \left| \vec{\mu} \right| \Psi_j \rangle = \left\langle i_1 i_2 i_3 \left| \vec{\mu}_0 + \sum_k \frac{\partial \vec{\mu}}{\partial Q_k} Q_k + \frac{1}{2} \sum_{kl} \frac{\partial^2 \vec{\mu}}{\partial Q_k Q_l} Q_k Q_l + \frac{1}{6} \sum_{klm} \frac{\partial^3 \vec{\mu}}{\partial Q_k Q_l Q_m} Q_k Q_l Q_m \right. \right.$$
$$\left. \left. + \frac{1}{24} \sum_{klmn} \frac{\partial^4 \vec{\mu}}{\partial Q_k Q_l Q_m Q_n} Q_k Q_l Q_m Q_n + \ldots \right| j_1 j_2 j_3 \right\rangle, \tag{16}$$

with the initial and final harmonic osillator eigenstates characterized by their quantum numbers i_1, i_2, i_3 and j_1, j_2, j_3, respectively. The position operator is rewritten using ladder operators as $Q_k = \sqrt{\frac{\hbar}{2m\omega_k}} \left(a + a^\dagger\right)$, yielding the following leading-order expressions for the one-quantum transitions

$$\langle i_1 i_2 i_3 \left| \vec{\mu} \right| (i_1 i_2 i_3) \pm 1 \rangle \propto \left\langle i_1 i_2 i_3 \left| \sum_k \frac{\partial \vec{\mu}}{\partial Q_k} \left(a_k + a_k^\dagger\right) \right| (i_1 i_2 i_3) \pm 1 \right\rangle, \tag{17}$$

where $(i_1 i_2 i_3) \pm 1$ indicates that either of the three states gains or loses one quantum of energy, for the two-quantum transitions,

$$\langle i_1 i_2 i_3 \left| \vec{\mu} \right| (i_1 i_2 i_3) \pm 2 \rangle \propto \left\langle i_1 i_2 i_3 \left| \frac{\partial^2 \vec{\mu}}{\partial Q_k Q_l} \left(a_k + a_k^\dagger\right) \left(a_l + a_l^\dagger\right) \right| (i_1 i_2 i_3) \pm 2 \right\rangle, \tag{18}$$

and similar equations for the three- and four-quantum transitions. Higher-order contributions are not included as they are small in all cases considered here. Additionally, all transitions involving more than two modes are not calculated as the matrix element for, e.g., a simultanous change of one quantum in both degenerate modes and the third mode is expected to be of similar magnitude as the matrix element for a simultanous change of two quanta in either of the degenerate modes and one quantum in the third mode. This was tested for two-quantum transitions where the matrix element for a change of one quantum in each of the two degenerate modes has a similar magnitude as the matrix element for changing two quanta in either of the two degenerate modes. Eqs. 7 and 8 are then employed to obtain the RDM matrix elements.

The derivatives of the dipole and polarizability along the normal modes Q_i are obtained from finite central differences[17] as

$$\frac{\partial f}{\partial Q_i} \approx \frac{1}{h_i}\left(\frac{-1}{60}f(\mathbf{x}-3h_i)+\frac{3}{20}f(\mathbf{x}-2h_i)+\frac{-3}{4}f(\mathbf{x}-h_i)\right.$$
$$\left.+\frac{3}{4}f(\mathbf{x}+h_i)+\frac{-3}{20}f(\mathbf{x}+2h_i)+\frac{1}{60}f(\mathbf{x}+3h_i)\right), \tag{19}$$

$$\frac{\partial f}{\partial Q_i^2} \approx \frac{1}{h_i^2}\left(\frac{1}{90}f(\mathbf{x}-3h_i)+\frac{-3}{20}f(\mathbf{x}-2h_i)+\frac{3}{2}f(\mathbf{x}-h_i)\right.$$
$$\left.\frac{-49}{18}f(\mathbf{x})+\frac{3}{2}f(\mathbf{x}+h_i)+\frac{-3}{20}f(\mathbf{x}+2h_i)+\frac{1}{90}f(\mathbf{x}+3h_i)\right), \tag{20}$$

$$\frac{\partial f}{\partial Q_i^3} \approx \frac{1}{h_i^3}\left(\frac{-7}{240}f(\mathbf{x}-4h_i)+\frac{3}{10}f(\mathbf{x}-3h_i)+\frac{-169}{120}f(\mathbf{x}-2h_i)+\frac{61}{30}f(\mathbf{x}-h_i)\right.$$
$$\left.+\frac{-61}{30}f(\mathbf{x}+h_i)+\frac{169}{120}f(\mathbf{x}+2h_i)+\frac{-3}{10}f(\mathbf{x}+3h_i)+\frac{7}{240}f(\mathbf{x}+4h_i)\right), \tag{21}$$

$$\frac{\partial f}{\partial Q_i^4} \approx \frac{1}{h_i^4}\left(\frac{7}{240}f(\mathbf{x}-4h_i)+\frac{-2}{5}f(\mathbf{x}-3h_i)+\frac{169}{60}f(\mathbf{x}-2h_i)+\frac{-122}{15}f(\mathbf{x}-h_i)\right.$$
$$\left.+\frac{91}{8}f(\mathbf{x})+\frac{-122}{15}f(\mathbf{x}+h_i)+\frac{169}{60}f(\mathbf{x}+2h_i)+\frac{-2}{5}f(\mathbf{x}+3h_i)+\frac{7}{240}f(\mathbf{x}+4h_i)\right), \tag{22}$$

where f is either the dipole or the polarizability, $\mathbf{x}$ is the minimum geometry and a step size of $h = 0.01\mathbf{x}_i$ was employed, where $\mathbf{x}_i$ is the Cartesian displacements of the i-th normal mode in bohr. Combinations of these terms are employed to obtain derivatives along several normal modes, e.g., to obtain $\frac{\partial f}{\partial Q_i \partial Q_j}$. Due to the factor $\frac{1}{h_i^4}$ the results for the fourth-order derivatives become numerically unstable and thus no results for four quantum transitions are shown here. To obtain the dipoles at each geometry we employ both *ab initio* calculations and calculations based on a DID model.

Ab Initio Electronic Structure Calculations

Ab initio electronic structure calculations are performed at the Hatree-Fock (HF), second-order Møller-Plesset perturbation theory (MP2), and coupled-cluster singles and doubles (CCSD) level employing an augmented triple zeta basis set developed by Dunning (aug-

cc-pVTZ).[16] All electronic structure calculations are performed using the Gaussian 09[18] package. Dipoles are calculated analytically for all three methods, and polarizabilities are calculated analytically for HF and MP2 and numerically for CCSD. In addition, density functional theory (DFT) calculations were performed, but the IR intensities of the low-frequency bromoform normal modes considered here showed a very strong dependence on the exchange-correlation functional and thus no DFT results are discussed.

Transition matrix elements are calculated for single bromoform molecules at their minimum energy geometry and for a bromoform cluster consisting of a central bromoform surrounded by the seven bromoforms in the first solvation shell. The geometry of the cluster is sampled from a MD trajectory. All geometries are provided in Tables S6 and S7. To obtain the derivatives of the dipole and polarizability along the normal modes in the cluster configuration, the HF minimum geometry as well as the corresponding normal modes of the bare (gas-phase) central molecule are employed and only the central molecule is allowed to move, while the surrounding bromoform moleculess are fixed. Thus, effects due to coupled inter-/intramolecular motions are neglected.

Dipole-Induced Dipole Model and MD Simulations

Additionally, we investigated non-linearities in the dipole and polarizability matrix elements based on ideas developed for classical MD force fields. Here, the dipoles and polarizabilities are calculated employing a dipole-induced dipole model (DID).[19–21] Dipoles and polarizabilities of a set of N atoms are calculated as

$$\alpha = \sum_{i=1}^{N} (A \cdot 1)_i \tag{23}$$

$$\mu = \sum_{i=1}^{N} \mu_i^{\text{perm}} + \sum_{i=1}^{N} (A \cdot E)_i \tag{24}$$

Table S6: Optimized geometries in bohr for isolated bromoform at the stated level of *ab initio* theory employing the aug-CC-pVTZ basis set and employing a MD force field (FF).

Atom	Coordinate	HF	MP2	CCSD	FF
C	x	0.000	0.000	0.000	0.000
C	y	0.000	0.000	0.000	0.000
C	z	0.979	0.994	0.988	-1.247
H	x	0.000	0.000	0.000	-0.019
H	y	0.000	0.000	0.000	0.019
H	z	2.998	3.037	3.027	-3.307
Br1	x	0.000	0.000	0.000	-3.402
Br1	y	3.478	3.455	3.468	-0.926
Br1	z	-0.084	-0.086	-0.085	-0.132
Br2	x	3.012	2.993	3.003	2.513
Br2	y	-1.739	-1.728	-1.734	-2.513
Br2	z	-0.084	-0.086	-0.085	-0.208
Br3	x	-3.012	-2.993	-3.003	0.907
Br3	y	-1.739	-1.728	-1.734	3.420
Br3	z	-0.084	-0.086	-0.085	-0.132

where the sum runs over the N 3×3 and 3×1 submatrices describing the polarizability and dipole of each atom, respectively. The $3N$×3 matrix 1 in Eq. 23 is defined as

$$1 = \begin{pmatrix} 1 & 0 & 0 \\ 0 & 1 & 0 \\ 0 & 0 & 1 \\ 1 & 0 & 0 \\ 0 & 1 & 0 \\ 1 & 0 & 1 \\ \vdots & \vdots & \vdots \end{pmatrix} \tag{25}$$

Table S7: Geometry in bohr of the bromoform cluster used in the *ab initio* calculations sampled from MD simulation. Each column refers to one of the bromoform molecules and the first column is the center molecule.

Atom	Coordinate	Center	1	2	3	4	5	6	7
C	x	0.000	5.238	8.789	0.778	-3.528	-0.863	-7.694	3.122
C	y	0.000	8.598	7.311	-8.390	2.116	-10.52	2.923	-1.814
C	z	0.979	-5.302	6.119	-5.009	7.588	8.951	-3.312	-9.299
H	x	0.000	6.910	7.757	2.846	-6.773	-2.854	-10.74	0.232
H	y	0.000	6.135	3.778	-11.05	3.822	-8.562	1.497	-0.762
H	z	2.998	-3.082	6.449	-3.474	7.079	6.512	-1.745	-7.232
Br1	x	0.000	5.901	8.789	3.907	-7.411	-4.694	-11.03	0.423
Br1	y	3.478	5.807	2.861	-11.88	4.839	-9.438	2.678	-1.230
Br1	z	-0.084	-1.306	7.992	-5.036	8.759	6.207	-0.759	-5.234
Br2	x	3.012	10.38	8.805	0.287	-9.551	-1.019	-11.00	-2.870
Br2	y	-1.739	7.095	1.936	-13.53	1.552	-8.346	-1.919	-2.376
Br2	z	-0.084	-2.234	3.410	-2.431	6.186	3.295	-0.348	-8.451
Br3	x	-3.012	7.293	4.162	5.276	-6.735	-3.740	-13.72	-0.528
Br3	y	-1.739	2.873	3.208	-9.897	6.268	-5.303	2.377	2.857
Br3	z	-0.084	-4.757	7.130	-0.910	4.309	8.021	-3.769	-7.454

and the $3N \times 3N$ matrix A is defined as

$$A^{-1} = \begin{pmatrix} \alpha_1^{-1} & T_{12} & T_{13} & \dots \\ T_{21} & \alpha_2^{-1} & T_{23} & \dots \\ T_{31} & T_{32} & \alpha_3^{-1} & \dots \\ \vdots & \vdots & \vdots & \vdots \end{pmatrix}, \tag{26}$$

(27)

where the α are isotropic atomic polarizabilities and

$$T_{ij} = \frac{\delta_{ij}}{\|r_{ij}\|^3} f_1(\|r_{ij}\|) - \frac{3 \cdot r_{ij} \otimes r_{ij}}{\|r_{ij}\|^5} f_2(\|r_{ij}\|), \tag{28}$$

$$f_1(x) = 1 - \left(\frac{a^2 x^2}{2} + ax + 1 \right) \mathrm{e}^{-ax}, \tag{29}$$

$$f_2(x) = 1 - \left(\frac{a^3 x^3}{6} + \frac{a^2 x^2}{2} + ax + 1 \right) \mathrm{e}^{-ax}. \tag{30}$$

Here r_{ij} is the vector between the i-th and j-th atom and a is the screening length. The $3N$ vector E contains the electric field at each atom

$$E = \begin{pmatrix} E_1 \\ E_2 \\ \vdots \end{pmatrix}, \tag{31}$$

with $E_j = \sum_i q_i \cdot f_1(\|r_{ij}\|) \cdot \frac{r_{ij}}{\|r_{ij}\|^3}$. The isotropic polarizabilities and the screening length are taken from Ref.[21] and summarized in Tab. S8.

Table S8: Parameters employed in the DID model taken from Ref.[21] (values in au).

Parameter	Value (au)
α_{C}	23.5714
α_{H}	2.7927
α_{Br}	8.6959
a	2.1304

The dipole and polarizability transition matrix elements obtained from these calculations are averaged over several geometries sampled from a long MD trajectory. MD simulations are performed using the GROMCAS package[22] and a GROMOS[23] based force field.[24] A simulation box of 256 molecules with the experimental density of 2.89 g/cm^3 was thermalized to 300 K employing the Nose-Hoover thermostat,[25] the velocity-Verlet integrator,[26] and a timestep of 0.5 fs. Periodic boundary conditions are used in all MD simulations and van-der-Wals interactions are smoothly switched off starting at 1.5 nm and set to zero at 1.66 nm, while Ewald sums are used to treat the long-range electrostatics. Configurations are then sampled from a long NVT trajectory every 5 ps to avoid artificial correlations.

The following strategy is employed to obtain the dipole and polarizability from a long MD trajectory:

1. For each sample time step and molecule extract a cluster surrounding that molecule (i.e. with center-of-mass to center-of-mass distance $< X = 6$ Å).

2. For each cluster, minimize the geometry of the central molecule, keeping all other molecules fixed.
3. For each central molecule, calculate the normal modes of the central molecule disregarding all surrounding molecules.
4. For each cluster, calculate the derivatives of the dipole moment/polarizability of the central molecule along its normal modes including effects induced by the surrounding cluster.

As in the electronic structure calculations, only the motion of the central molecule is considered, the first solvation shell is fixed. Several different variants of this protocol were tested, but the results did not differ significantly. For example:

- Different cluster sizes ($X = 10$ Å, 30 Å) were employed.
- The minimization in step two was omitted.
- The normal modes obtained in step three were calculated taking all surrounding molecules into account.
- The dipole and polarizability of the full cluster were calculated including all induced effects.

Different combinations of these variants were also tested.

Ab Initio Results for Isolated Bromoform

Tables S3 and S4 summarize the results obtained for the transition dipole and transition polarizability matrix elements of a single bromoform molecule at the different levels of theory employed. To allow for a better comparison with the values obtain from the RDM analysis, all values are scaled by the $\langle 001 \,|f|\, 000 \rangle$ matrix element. All non-linearities in the transition dipole matrix elements are significantly smaller than those obtained from the RDM analysis. For the transition polarizability matrix elements no significant non-linearities are found, in accord with the RDM analysis of the experimental spectrum.

Ab Initio Results for a Bromoform Cluster

In Tables S9 and S10 the results for a bromoform cluster are presented at the HF and MP2 level of theory. Here, a step size of $h = 0.02\mathbf{x}_i$ is employed. To obtain results with MP2 for the cluster case, the lanl2dz[27] effective core potential is employed. Again, no significant non-linearities in the transition dipole nor in the transition polarizability matrix elements are found. As these calculations become very costly, it was not possible to obtain results for a more representative sample of liquid bromoform configurations. It is conceivable that the experimental results are sensitive only to a subset of liquid configurations that show significant non-linearities.

Table S9: Calculated dipole matrix elements for a cluster of eight $CHBr_3$ molecules.

States	Quanta	HF	MP2
$\|0\ 0\ 0\ \rangle$, $\|1\ 0\ 0\ \rangle$	1	1.000	1.000
$\|0\ 0\ 0\ \rangle$, $\|0\ 1\ 0\ \rangle$	1	0.411	3.230
$\|0\ 0\ 0\ \rangle$, $\|0\ 0\ 1\ \rangle$	1	1.880	2.647
$\|1\ 0\ 0\ \rangle$, $\|0\ 0\ 1\ \rangle$	2	0.040	0.081
$\|0\ 1\ 0\ \rangle$, $\|0\ 0\ 1\ \rangle$	2	0.030	0.028
$\|2\ 0\ 0\ \rangle$, $\|1\ 0\ 1\ \rangle$	2	0.056	0.115
$\|0\ 2\ 0\ \rangle$, $\|0\ 1\ 1\ \rangle$	2	0.042	0.040
$\|1\ 1\ 0\ \rangle$, $\|1\ 0\ 1\ \rangle$	2	0.030	0.028
$\|1\ 1\ 0\ \rangle$, $\|0\ 1\ 1\ \rangle$	2	0.040	0.081
$\|1\ 0\ 1\ \rangle$, $\|0\ 0\ 2\ \rangle$	2	0.056	0.115
$\|0\ 1\ 1\ \rangle$, $\|0\ 0\ 2\ \rangle$	2	0.042	0.040
$\|1\ 0\ 0\ \rangle$, $\|0\ 0\ 2\ \rangle$	3	0.048	0.003
$\|0\ 1\ 0\ \rangle$, $\|0\ 0\ 2\ \rangle$	3	0.009	0.006
$\|0\ 0\ 1\ \rangle$, $\|2\ 0\ 0\ \rangle$	3	0.014	0.010
$\|0\ 0\ 1\ \rangle$, $\|0\ 2\ 0\ \rangle$	3	0.003	0.010
$\|0\ 0\ 1\ \rangle$, $\|1\ 1\ 0\ \rangle$	3	0.000	0.000
$\|1\ 0\ 1\ \rangle$, $\|3\ 0\ 0\ \rangle$	3	0.025	0.018
$\|0\ 1\ 1\ \rangle$, $\|0\ 3\ 0\ \rangle$	3	0.006	0.018
$\|1\ 0\ 1\ \rangle$, $\|2\ 1\ 0\ \rangle$	3	0.000	0.000
$\|1\ 0\ 1\ \rangle$, $\|1\ 2\ 0\ \rangle$	3	0.003	0.010
$\|0\ 1\ 1\ \rangle$, $\|1\ 2\ 0\ \rangle$	3	0.000	0.000
$\|0\ 1\ 1\ \rangle$, $\|2\ 1\ 0\ \rangle$	3	0.014	0.010

Table S10: Calculated polarizability matrix elements for a cluster of eight $CHBr_3$ molecules.

States	Quanta	HF	MP2
$\|0\ 0\ 0\ \rangle$, $\|1\ 0\ 0\ \rangle$	1	1.000	1.000
$\|0\ 0\ 0\ \rangle$, $\|0\ 1\ 0\ \rangle$	1	0.937	1.036
$\|0\ 0\ 0\ \rangle$, $\|0\ 0\ 1\ \rangle$	1	0.926	0.846
$\|1\ 0\ 0\ \rangle$, $\|0\ 0\ 1\ \rangle$	2	0.025	0.008
$\|0\ 1\ 0\ \rangle$, $\|0\ 0\ 1\ \rangle$	2	0.023	0.010
$\|2\ 0\ 0\ \rangle$, $\|1\ 0\ 1\ \rangle$	2	0.036	0.012
$\|0\ 2\ 0\ \rangle$, $\|0\ 1\ 1\ \rangle$	2	0.032	0.014
$\|1\ 1\ 0\ \rangle$, $\|1\ 0\ 1\ \rangle$	2	0.023	0.010
$\|1\ 1\ 0\ \rangle$, $\|0\ 1\ 1\ \rangle$	2	0.025	0.008
$\|1\ 0\ 1\ \rangle$, $\|0\ 0\ 2\ \rangle$	2	0.036	0.012
$\|0\ 1\ 1\ \rangle$, $\|0\ 0\ 2\ \rangle$	2	0.032	0.014
$\|1\ 0\ 0\ \rangle$, $\|0\ 0\ 2\ \rangle$	3	0.001	0.000
$\|0\ 1\ 0\ \rangle$, $\|0\ 0\ 2\ \rangle$	3	0.001	0.000
$\|0\ 0\ 1\ \rangle$, $\|2\ 0\ 0\ \rangle$	3	0.000	0.000
$\|0\ 0\ 1\ \rangle$, $\|0\ 2\ 0\ \rangle$	3	0.000	0.000
$\|0\ 0\ 1\ \rangle$, $\|1\ 1\ 0\ \rangle$	3	0.000	0.000
$\|1\ 0\ 1\ \rangle$, $\|3\ 0\ 0\ \rangle$	3	0.001	0.000
$\|0\ 1\ 1\ \rangle$, $\|0\ 3\ 0\ \rangle$	3	0.001	0.000
$\|1\ 0\ 1\ \rangle$, $\|2\ 1\ 0\ \rangle$	3	0.000	0.000
$\|1\ 0\ 1\ \rangle$, $\|1\ 2\ 0\ \rangle$	3	0.000	0.000
$\|0\ 1\ 1\ \rangle$, $\|1\ 2\ 0\ \rangle$	3	0.000	0.000
$\|0\ 1\ 1\ \rangle$, $\|2\ 1\ 0\ \rangle$	3	0.000	0.000

Dipole-Induced Dipole Results

In this section, the results obtain from the DID model described in Sec. are presented. In Tables S3 and S4 the transition dipole and transition polarizability matrix elements for the RDM model are shown for a single bromoform molecule at the optimized geometry for the GROMOS based force field (see Tab. S6). No significant non-linearities are found. Indeed, the values obtained are even smaller than those predicted by the *ab initio* calculations.

Tables S11 and S12 present the values for the transition dipole and transition polarizability matrix elements obtained by employing the strategy devised in Sec. and averaging over a total of 2560 bromoform clusters sampled at ten different times in the MD trajectory. As before, no significant non-linearities in the matrix elements are found.

Table S11: Calculated dipole matrix elements employing the DID model and sampling 2560 cluster configurations.

States	Quanta	DID
$\|0\ 0\ 0\rangle$, $\|1\ 0\ 0\rangle$	1	1.00
$\|0\ 0\ 0\rangle$, $\|0\ 1\ 0\rangle$	1	0.93
$\|0\ 0\ 0\rangle$, $\|0\ 0\ 1\rangle$	1	1.07
$\|1\ 0\ 0\rangle$, $\|0\ 0\ 1\rangle$	2	0.01
$\|0\ 1\ 0\rangle$, $\|0\ 0\ 1\rangle$	2	0.01
$\|2\ 0\ 0\rangle$, $\|1\ 0\ 1\rangle$	2	0.01
$\|0\ 2\ 0\rangle$, $\|0\ 1\ 1\rangle$	2	0.01
$\|1\ 1\ 0\rangle$, $\|1\ 0\ 1\rangle$	2	0.01
$\|1\ 1\ 0\rangle$, $\|0\ 1\ 1\rangle$	2	0.01
$\|1\ 0\ 1\rangle$, $\|0\ 0\ 2\rangle$	2	0.01
$\|0\ 1\ 1\rangle$, $\|0\ 0\ 2\rangle$	2	0.01
$\|1\ 0\ 0\rangle$, $\|0\ 0\ 2\rangle$	3	0.00
$\|0\ 1\ 0\rangle$, $\|0\ 0\ 2\rangle$	3	0.00
$\|0\ 0\ 1\rangle$, $\|2\ 0\ 0\rangle$	3	0.00
$\|0\ 0\ 1\rangle$, $\|0\ 2\ 0\rangle$	3	0.00
$\|0\ 0\ 1\rangle$, $\|1\ 1\ 0\rangle$	3	0.00
$\|1\ 0\ 1\rangle$, $\|3\ 0\ 0\rangle$	3	0.00
$\|0\ 1\ 1\rangle$, $\|0\ 3\ 0\rangle$	3	0.00
$\|1\ 0\ 1\rangle$, $\|2\ 1\ 0\rangle$	3	0.00
$\|1\ 0\ 1\rangle$, $\|1\ 2\ 0\rangle$	3	0.00
$\|0\ 1\ 1\rangle$, $\|1\ 2\ 0\rangle$	3	0.00
$\|0\ 1\ 1\rangle$, $\|2\ 1\ 0\rangle$	3	0.00

Table S12: Calculated polarizability matrix elements employing the DID model and sampling 2560 cluster configurations.

States	Quanta	DID
$\|0\ 0\ 0\rangle$, $\|1\ 0\ 0\rangle$	1	1.00
$\|0\ 0\ 0\rangle$, $\|0\ 1\ 0\rangle$	1	0.96
$\|0\ 0\ 0\rangle$, $\|0\ 0\ 1\rangle$	1	0.23
$\|1\ 0\ 0\rangle$, $\|0\ 0\ 1\rangle$	2	0.01
$\|0\ 1\ 0\rangle$, $\|0\ 0\ 1\rangle$	2	0.01
$\|2\ 0\ 0\rangle$, $\|1\ 0\ 1\rangle$	2	0.02
$\|0\ 2\ 0\rangle$, $\|0\ 1\ 1\rangle$	2	0.02
$\|1\ 1\ 0\rangle$, $\|1\ 0\ 1\rangle$	2	0.01
$\|1\ 1\ 0\rangle$, $\|0\ 1\ 1\rangle$	2	0.01
$\|1\ 0\ 1\rangle$, $\|0\ 0\ 2\rangle$	2	0.02
$\|0\ 1\ 1\rangle$, $\|0\ 0\ 2\rangle$	2	0.02
$\|1\ 0\ 0\rangle$, $\|0\ 0\ 2\rangle$	3	0.00
$\|0\ 1\ 0\rangle$, $\|0\ 0\ 2\rangle$	3	0.00
$\|0\ 0\ 1\rangle$, $\|2\ 0\ 0\rangle$	3	0.00
$\|0\ 0\ 1\rangle$, $\|0\ 2\ 0\rangle$	3	0.00
$\|0\ 0\ 1\rangle$, $\|1\ 1\ 0\rangle$	3	0.00
$\|1\ 0\ 1\rangle$, $\|3\ 0\ 0\rangle$	3	0.00
$\|0\ 1\ 1\rangle$, $\|0\ 3\ 0\rangle$	3	0.00
$\|1\ 0\ 1\rangle$, $\|2\ 1\ 0\rangle$	3	0.00
$\|1\ 0\ 1\rangle$, $\|1\ 2\ 0\rangle$	3	0.00
$\|0\ 1\ 1\rangle$, $\|1\ 2\ 0\rangle$	3	0.00
$\|0\ 1\ 1\rangle$, $\|2\ 1\ 0\rangle$	3	0.00

Discussion of Electronic Structure and MD Results

Transition dipole and polarizability matrix elements were calculated employing *ab inito* electronic structure calculations and MD simulations in combination with a dipole-induced dipole model. The matrix elements obtained for isolated bromoform with these strategies show no non-linearities in the transition matrix elements. This is in contrast to the analysis of the experimental spectrum employing the RDM model. This suggests that peaks in the experimentally observed spectrum are due to effects of the liquid environment.

Interestingly, the *ab initio* electronic structure calculations performed for a bromoform cluster also yield no non-linearities in the transition dipole and polarizability matrix elements. Due to the high computational cost of these calculations, only one cluster configuration was considered. The experiments, however, might be sensitive to just a small fraction of the liquid configurations that show non-linearities.

To more systematically explore other solvent configurations, transition dipole and polarizability matrix elements were calculated using a DID model and averaging over 2560 bromoform clusters sampled from a MD simulation. No significant non-linearities were found. Inaccuracies in the parameters of the employed force field, e.g., inaccuracies in the vibrational frequencies, in the Lennard-Jones parameters, and in the partial charges, might cause an incorrect sampling of the geometries. In addition, shortcomings in the DID model, e.g., the neglect of charge-transfer, the approximate description of induced effects, as well as incorrect DID parameters and the neglect of long-range effects in the DID calculations presented, might also cause the non-linearities to be small.

Moreover, all of the theoretical strategies employed in this work ignore coupled motion of different bromoform molecules when calculating the derivatives of the dipole and polarizability. We note that the normal modes describing hindered translation and rotation have frequencies up to 90 cm^{-1}. Thus, the coupling of low-lying intramolecular vibrational states and the intermolecular modes supported by the liquid might be important. The different strategies employed in this work did not show any nonlinearities in the transition dipole and

polarizability matrix elements, which suggests that the coupled motion of several bromoform monomers might be the source of the nonlinearities in the transition dipole matrix elements leading to the peaks in the experimentally observed spectrum.

References

(1) Finneran, I. A.; Welsch, R.; Allodi, M. A.; Miller, T. F.; Blake, G. A. Coherent Two-Dimensional Terahertz-Terahertz-Raman Spectroscopy. *Proc. Natl. Acad. Sci. U.S.A.* **2016**, *113*, 6857–6861.

(2) Allodi, M. A.; Finneran, I. A.; Blake, G. A. Nonlinear Terahertz Coherent Excitation of Vibrational Modes of Liquids. *J. Chem. Phys.* **2015**, *143*, 234204.

(3) Leforestier, C.; Bisseling, R.; Cerjan, C.; Feit, M.; Friesner, R.; Guldberg, A.; Hammerich, A.; Jolicard, G.; Karrlein, W.; Meyer, H.-D. et al. A Comparison of Different Propagation Schemes for the Time Dependent Schrdinger Equation. *J. Comput. Phys.* **1991**, *94*, 59 – 80.

(4) Mukamel, S. *Principles of Nonlinear Optical Spectroscopy*; Oxford University Press: New York, U.S.A., 1999.

(5) Hamm, P.; Zanni, M. *Concepts and Methods of 2D Infrared Spectroscopy*; Cambridge University Press: New York, U.S.A., 2011.

(6) Bernath, P. F. *Spectra of Atoms and Molecules*; Oxford University Press: New York, U.S.A., 2015.

(7) Ratajczak, H.; Ford, T.; Orville-Thomas, W. Infrared Dispersion Studies: 11. Band Intensities and Vibrational Polarizations of Chloroform, Bromoform and their Deuterated Analogues. *J. Mol. Struct.* **1972**, *14*, 281–291.

(8) Wales, D. J.; Doye, J. P. Global Optimization by Basin-Hopping and the Lowest Energy Structures of Lennard-Jones Clusters Containing up to 110 Atoms. *J. Phys. Chem. A* **1997**, *101*, 5111–5116.

(9) Perez, R. E.; Jansen, P. W.; Martins, J. R. R. A. pyOpt: A Python-Based Object-Oriented Framework for Nonlinear Constrained Optimization. *Struct. Multidiscipl. Optim.* **2012**, *45*, 101–118.

(10) Khalil, M.; Demirdöven, N.; Tokmakoff, A. Vibrational Coherence Transfer Characterized with Fourier-Transform 2D IR Spectroscopy. *J. Chem. Phys.* **2004**, *121*, 362–373.

(11) Baiz, C. R.; Kubarych, K. J.; Geva, E. Molecular Theory and Simulation of Coherence Transfer in Metal Carbonyls and Its Signature on Multidimensional Infrared Spectra. *J. Phys. Chem. B* **2011**, *115*, 5322–5339.

(12) Nielsen, H. H. The Vibration-Rotation Energies of Molecules. *Rev. Mod. Phys.* **1951**, *23*, 90–136.

(13) Bloino, J.; Barone, V. A Second-Order Perturbation Theory Route to Vibrational Averages and Transition Properties of Molecules: General Formulation and Application to Infrared and Vibrational Circular Dichroism Spectroscopies. *J. Chem. Phys.* **2012**, *136*, 124108.

(14) Bloino, J. A VPT2 Route to Near-Infrared Spectroscopy: The Role of Mechanical and Electrical Anharmonicity. *J. Phys. Chem. A* **2015**, *119*, 5269–5287.

(15) Frisch, M. J.; Trucks, G. W.; Schlegel, H. B.; Scuseria, G. E.; Robb, M. A.; Cheeseman, J. R.; Scalmani, G.; Barone, V.; Petersson, G. A.; Nakatsuji, H. et al. Gaussian 16 Revision A.03. 2016; Gaussian Inc. Wallingford CT.

(16) Kendall, R. A.; Dunning Jr, T. H.; Harrison, R. J. Electron Affinities of the First-Row

Atoms Revisited. Systematic Basis Sets and Wave Functions. *J. Chem. Phys.* **1992**, *96*, 6796–6806.

(17) Fornberg, B. Generation of Finite Difference Formulas on Arbitrarily Spaced Grids. *Math. Comp.* **1988**, *51*, 699–706.

(18) Frisch, M. J.; Trucks, G. W.; Schlegel, H. B.; Scuseria, G. E.; Robb, M. A.; Cheeseman, J. R.; Scalmani, G.; Barone, V.; Mennucci, B.; Petersson, G. A. et al. Gaussian 09 Revision D.01. Gaussian Inc. Wallingford CT 2009.

(19) Thole, B. T. Molecular Polarizabilities Calculated with a Modified Dipole Interaction. *Chem. Phys.* **1981**, *59*, 341–350.

(20) Bellido, M. On the Polarizability of the Sulfur Atom. *Chem. Phys. Lett.* **1985**, *122*, 562–566.

(21) Van Duijnen, P. T.; Swart, M. Molecular and Atomic Polarizabilities: Thole's Model Revisited. *J. Phys. Chem. A* **1998**, *102*, 2399–2407.

(22) Berendsen, H. J.; van der Spoel, D.; van Drunen, R. GROMACS: A Message-Passing Parallel Molecular Dynamics Implementation. *Comput. Phys. Commun.* **1995**, *91*, 43–56.

(23) Schmid, N.; Eichenberger, A. P.; Choutko, A.; Riniker, S.; Winger, M.; Mark, A. E.; van Gunsteren, W. F. Definition and Testing of the GROMOS Force-Field Versions 54A7 and 54B7. *Eur. Biophys. J.* **2011**, *40*, 843–856.

(24) Malde, A. K.; Zuo, L.; Breeze, M.; Stroet, M.; Poger, D.; Nair, P. C.; Oostenbrink, C.; Mark, A. E. An Automated Force Field Topology Builder (ATB) and Repository: Version 1.0. *J. Chem. Theory Comput.* **2011**, *7*, 4026–4037.

(25) Hoover, W. G. Canonical Dynamics: Equilibrium Phase-Space Distributions. *Phys. Rev. A* **1985**, *31*, 1695–1697.

(26) Swope, W. C.; Andersen, H. C.; Berens, P. H.; Wilson, K. R. A Computer Simulation Method for the Calculation of Equilibrium Constants for the Formation of Physical Clusters of Molecules: Application to Small Water Clusters. *J. Chem. Phys.* **1982**, *76*, 637–649.

(27) Hay, P. J.; Wadt, W. R. Ab Initio Effective Core Potentials for Molecular Calculations. Potentials for K to Au Including the Outermost Core Orbitals. *J. Chem. Phys.* **1985**, *82*, 299–310.